Simulation of a latent heat thermal energy storage
for the solar air-conditioning system of a net-zero energy hotel

BYRNE PAUL, LALANNE PASCAL
Laboratoire Génie Civil Génie Mécanique
Université de Rennes
IUT GCCD, 3 rue du Clos Courtel BP 90422, 35704 Rennes Cedex 7
FRANCE
paul.byrne@univ-rennes1.fr

Abstract: - Hotels consume a large amount of energy for air-conditioning, especially in hot regions of the world. In the context of climate change, improvements can be made using the concept of net-zero energy (NZE) buildings. Renewable energy enables to satisfy this objective. In this article, a literature review justifies the use of a solar photovoltaic air-conditioning (PV AC) system coupled to a latent heat thermal energy storage (LHTES). The LHTES uses fatty acids derived from coconut oil embedded in a compressed expanded matrix to enhance the apparent thermal conductivity of the composite up to 20 $W.m^{-1}.K^{-1}$. A simple simulation tool was developed to evaluate the melting time, in different configurations of LHTES for assisting design engineers. PCM in shell-and-tube configuration (tube spacing of 20 cm, tube diameter of 60 mm), slab-like configuration (thickness of 24 mm) and beam-like configuration (edge length of 39 mm melt in less than 6 hours. This study shows the possibility of storing cooling energy in a large LHTES.

Key-Words: - phase change material, graphite, LHTES, solar air-conditioning

1 Introduction

Air-conditioning is the major energy consumption in hotels under hot climates. It accounted for 32 % of electricity consumption of buildings in India and for 33 % in the subtropical Hong Kong in 2006 [1]. Isaac et al. predicts a 72 % increase of energy demand for cooling between the years 2000 and 2100 due to climate change [2]. From a sample of 16 hotels at Hong-Kong, around 45% of electricity consumption is due to air-conditioning (AC) [3]. Solar air-conditioning can be an interesting solution to reduce the environmental impact of the building during exploitation and dependency to the electric grid. However, air-conditioning demand still exist during the night under hot climates and solar energy needs to be stored to satisfy nocturnal duties [4]. Li et al. studied the sensitivity of design parameters and optimal design for zero/low energy buildings in subtropical regions [5]. The commonly optimized parameters are insulation thickness of the external walls, building orientation, a rather low window to wall ratio, efficient glazing type, sufficient external shading and a low value of wall solar absorbance. D'Agostino et al. also insists on the building envelope thermal capacity to store heat in order to

reduce significantly and delay temperature peaks inside the building [6]. In this study, the reduction of primary energy consumption and CO2 emissions can be maximized for hotels compared to other types of buildings.

The project presented in this article is a hotel in Lombok having the perspective of being net-zero energy. The objective is to ensure comfort to clients in the most environment-friendly manner. Solar photovoltaic (PV) coupled to vapour compression AC is preferred to solar thermal cooling technology because a PV field is planned to satisfy the electricity demand on site and because of the actually proved economic advantage of solar PV cooling [7]. Indeed, investment costs are much higher for solar thermal technology and its absorption or adsorption chiller would as well require the availability of skilled technicians.

Buildings deprived of storage that are offloading renewable electricity to the power grid and buying-back to balance their consumption do emit a large amount of CO2 because of a daily time-gap that forces power plants to burn fossil fuel at peaks during evenings [8]. Therefore, hotels claiming to be truly net-zero energy should not rely on the electric grid to reach this objective. An energy

storage system has to be employed to gain self reliance [9]. Hasnain [10] and Bourne and Novoselac [11] show the following advantages of a cold storage system compared to a conventional AC system:

- Reduction of plant capacity,
- Operation of compressor at full capacity for longer durations,
- Adjustment of the maximum of operational times during cheaper electricity or favourable climatic conditions,
- Coupling of AC systems around one cool storage should reduce the piping and the number of auxiliary devices.

These advantages lead to energy savings or running-cost savings and are accompanied with environmental benefits regarding greenhouse gas emissions due to the reduction of electricity consumption and or refrigerant charge. The main drawback is the investment cost, especially for a solar AC system since solar panels do not produce energy nightly. Indeed, the thermal capacity of the AC system must be sufficient to satisfy the actual thermal demand plus to store some energy for the night. This operation induces an oversizing compared to the solution of just the combination of an AC system and a cold storage connected to the electric grid.

In the objective of lowest environmental impact, the project aims as well to minimize the use of electric batteries. Luthander et al. [12] confirm that batteries are relatively expensive, have a limited life duration, lose a significant part of the stored energy by Joule effect during a loading-unloading process and have a high environmental impact because of the rare metals they contain and of the construction processes they employ. A thermal energy storage is thus preferred for the solar AC system.

The use of a PCM is a solution to reduce storage volume. PCMs can be classified into three categories: pure inorganic such as salt hydrates, pure organic such as paraffins and fatty acids or mixtures of inorganic and/or organic substances. The PCM chosen in the present study is a eutectic mixture of capric acid (decanoic) and lauric acid (dodecanoic). The mixture forms an eutectic and has its lower fusion temperature at around 18 °C when molar fractions are equal to 73 % of capric acid and 27 % of lauric acid, corresponding to around 70 % and 30% in mass proportions [13]. The composition of the eutectic mixture was investigated and certified by Longfei et al. [14]. The main reason for this choice of PCM is that these fatty acids are components of coconut oil. This aspect is environment-friendly and commercial. Hotel guests would probably be confused if the PCM was made of paraffins, mostly issued from petroleum distillation. As salt hydrates are not as well known as coconut oil by the public and cannot be bio-sourced they hold less educational benefit than coconut oil components.

Fauzi et al. [15] studied the benefits of a surfactant, sodium laurate, with a loading of 10 % in mass that should reduce the fusion temperature of the above mixture by 3 or 4 K. It should also reduce the difference between the starting and finishing temperature of fusion down to 2 K and increase slightly the latent heat of the PCM mixture. Other additives are excluded due to risks of rancidification regarding oleins, or of increasing the temperature interval of fusion or solidification. A large interval between these two temperatures would generate a decrease of the COP of the cooling system during the solidification stage.

The main drawback of PCMs is their low thermal conductivity [9], affecting thermal diffusivity and concretely the time needed to melt or solidify the material. Many ways to enhance the conductivity of PCMs were reviewed by Badenhorst [16] and Lin et al. [17]: metallic fins, nanoparticles (studied by Putra et al. [18]), graphite foam, expanded graphite (EG). One of the cheapest solution seems to be the use of EG. Graphite is a cheap material compared to nanoparticles or to the cost of manufacturing finned tubes or foams. From Mallow et al. [19] and Krzesinska [20-21] EG can also be compressed in one direction (through the plane, direction z) to form compressed expanded graphite (CEG), creating anisotropy inside the material. Electric and thermal conductivity are similarly enhanced in directions x and y (in the plane) (using x-y-z orthonormal vectors).

Latent heat thermal energy storage (LHTES) configurations are presented in several literature reviews [22-25]. The main ones are shell-and-tube heat exchangers, finned coil embedded in a case filled up with PCM, capsules, packed beds or plates. Merlin worked on a cooling energy storage of 100 kW for milk sterilisation [26]. The configuration studied corresponds to the shell-and-tube one. D'Avignon and Kummert worked on an experimental full-scale LHTES of around 30 kW as a maximum thermal power, containing stacks of slab-like PCM capsules [27].

Bie et al.[4] used computational fluid dynamic simulations to design a LHTES. They also recently made the same conclusion regarding energy savings with the help of renewables and LHTES for the application of heat recovery from industrial plants. However, their model uses commercial codes that are not always easily affordable. The possible configurations are studied in this article with a very simple simulation model for a quick assessment by researchers and design engineers. This model is even simpler than the simplified model of Fornarelli et al. [28], which actually simulates the natural convection in the liquid phase to obtain an accurate assessment. The present model does not take into account the natural convection because the chosen CEG does not offer the freedom to the liquid to activate convection in the small pores of the matrix. However, it was validated by comparison with the following results:

experimental results from

- Gasia et al. [29]: paraffin RT58, shell-and-tube configuration,
- D'Avignon and Kummert [27]: salt hydrate S27, flat plate configuration,
- Merlin [26]: paraffin RT60, shell-and-tube configuration,
- and Trp [30]: paraffin RT30, shell-and-tube configuration,

and simulation results from

- Youssef [31]: organic paraffin type A16, model of spiral-wired tubes,
- and Younsi [32]: salt hydrate S27, semi-infinite model.

The literature review of articles in the fields of hotels, solar air-conditioning and latent heat thermal energy storage (LHTES) lead this study towards a specific system. The solar air-conditioning system is described in the next section. The third part of this article focusses on the simulation model used to design the LHTES in unidimensional (1D) or radial configurations. The model is described then validated with varied conditions and operated to determine the most interesting LHTES configurations.

2 Description of the solar AC system

The studied AC system works with solar photovoltaic energy part of the day. The surplus of energy is used to store cooling energy in the LHTES. Starting from the first dark hours of the evening, the LHTES is discharging its cooling energy within the distribution network supplying terminal units inside hotel bedrooms. Optionally, during the second half of the night, the cooling energy could be brought freely by over-ventilation with outdoor air. The building thermal inertia should also participate to limit the indoor temperature increase related to internal gains. Figure 1 shows the general scheme. The PCM eutectic mixture of capric acid and lauric acid with 73 % and 27 % of molar fractions and with 10 % of sodium laurate as a surfactant shall have a fusion temperature of 16 °C, and have melting and solidification ranges of 2 K. The temperature regimes (inlet / outlet temperature in the LHTES) during charging (solidification during the day) and discharging (melting during the night) are 10 °C / 13 °C and 22 °C / 19 °C respectively. The charging temperature regime is interesting compared to an ice storage using water freezing at 0 °C because it is higher. The COP of the chiller should be significantly improved. The temperature regime during discharging is quite high compared to standard AC systems. This imposes a very high-quality insulation and envelope airtightness, which are usually required for net-zero energy buildings, and also for passive houses. The condensing fluid of the chiller unit can optionally be water from a large volume of swimming pool. This possibility could eventually enhance the COP compared to the COP of a chiller using an air-cooled condenser.

The storage system is composed of PCM impregnated inside an EG matrix. However, the carbon loading and the LHTES configuration are important parameters. The duration of a complete melting or solidification is targeted to 6 hours to leave the remaining part of the night to carry out optional free cooling. The objective of the simulation study is to determine the minimum thermal conductivity of the composite EG-PCM with different carbon loadings and different LHTES configurations to satisfy the criterion of 6 hours. Tables 1 and 2 indicate thermal properties of the selected PCM including effects of the surfactant as well as thermal properties of the graphite matrix. Liquid and solid phases of the PCM show very close values. The composite material properties are calculated by a mixing law. The model described by Bhattacharya et al. (provided through equations (1) to (3)) calculates the effective thermal conductivity of the composite, with PCM either in solid or liquid state, by combining a series model and a parallel model [33]. This model is valid for an isotropic material. The A factor has a constant value of 0.35. λ_x and $\lambda_\parallel$ are the effective thermal conductivities of the series model and of the parallel model respectively. ϵ is the porosity of the expanded

graphite matrix. The series and parallel conductivities combine three layers of PCM, graphite and air. The amount of air trapped inside the closed porosity of the composite material is assumed to represent 5 % of the total volume of the composite material. The properties of air at 20 °C are given in table 3.

$$\lambda_{comp} = A\lambda_{||} + (1 - A)\lambda_{\times} \qquad (1)$$

$$\lambda_{\times} = \frac{1}{\left(\frac{\varepsilon - 5\%}{\lambda_{PCM}} + \frac{1-\varepsilon}{\lambda_{EG}} + \frac{5\%}{\lambda_{air}}\right)} \qquad (2)$$

$$\lambda_{||} = (\varepsilon - 5\%)\lambda_{PCM} + (1 - \varepsilon)\lambda_{EG} + 5\%\lambda_{air} \qquad (3)$$
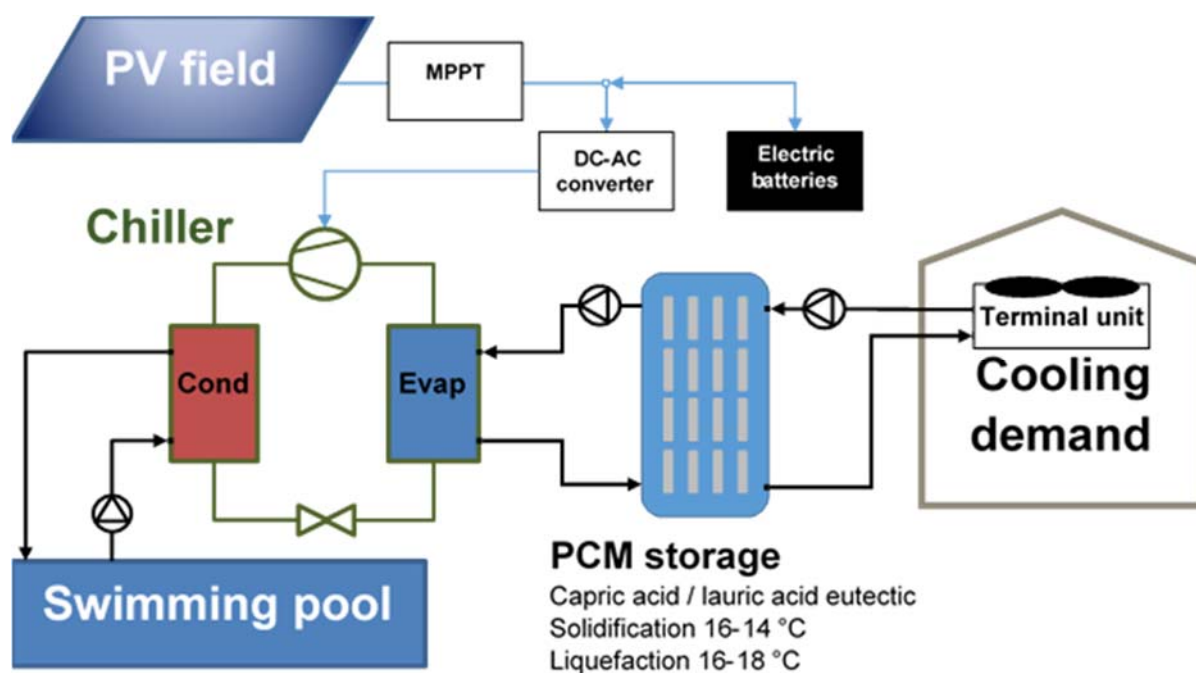
Figure 1: Scheme of the solar air-conditioning system with LHTES

Table 1: Thermal properties of PCM

Property	Value
Fusion temperature	16 °C
Latent heat	140 kJ.kg^{-1}
Specific heat of solid and liquid	2000 J.kg^{-1}.K^{-1}
Density of solid and liquid	900 kg.m^{-3}
Thermal conductivity of solid and liquid	0.18 W.m^{-1}.K^{-1}

Table 2: Thermal properties of graphite

Property	Value
Specific heat	710 J.kg^{-1}.K^{-1}
Density	2200 kg.m^{-3}
Thermal conductivity	500 W.m^{-1}.K^{-1}

Table 3: Thermal properties of air

Property	Value
Specific heat	1000 J.kg^{-1}.K^{-1}
Density	1.2 kg.m^{-3}
Thermal conductivity	0.02 W.m^{-1}.K^{-1}

Table 4 presents the variation of the thermal properties of the isotropic EG-PCM composite material. The first column corresponds to the PCM without carbon and without the contribution of trapped air. Other columns show a gradual increase of thermal conductivity λ of composite, of thermal diffusivity α and EG density possibly obtained by compression to create compressed expanded graphite (CEG). However, the specific heat and the latent heat expressed in MJ.m-3 decrease.

Table 4: Thermal properties of the PCM and the EG-PCM composite depending on the carbon loading

carbon loading (% in mass)	0	5	10	15	20	25	30
PCM volume percentage	100%	93.00%	90.90%	88.60%	86.20%	83.60%	80.80%
λ (W.m^{-2}.K^{-1})	0.18	3.65	7.37	11.34	15.57	20.09	24.94
ρ_{comp} (kg.m^{-3})	900	881	909	938	970	1003	1039
Cp (J.kg^{-1}.K^{-1})	2000	1924	1897	1867	1836	1803	1767
α (m^2.s^{-1})	1.00E-07	2.15E-06	4.28E-06	6.47E-06	8.74E-06	1.11E-05	1.36E-05
ρ_{EG} (kg.m^{-3})	0	44.1	90.9	140.7	193.9	250.8	311.8
Latent heat (MJ.m^{-3})	126.0	117.2	114.5	111.7	108.6	105.3	101.8

3 Simulation study

Dutil et al. carried out a thorough review of PCM simulation models [34]. They organized their study following the possible geometries of the PCM system: rectangular, cylindrical and spherical. The rectangular geometry applies to the space interval between two fins or to packed beds. The cylindrical geometry applies to shell-and-tube LHTES and the spherical geometry applies to capsules used in tanks or slurries. This section presents the unidimensional and radial models. The validation procedure is detailed hereafter. A simulation study is led to determine the best LHTES configurations depending on different parameters.

3.1 Description of the model

In the present study regarding high capacity storage such as packed beds or shell-and-tube, a one-dimension (1D) and a radial simulation models were developed based on the heat equation. The finite difference method enables to convert the derivatives into differences over time steps and space elements. The 1D heat equation is given in equation (4). Equation (5) converts the latter into finite differences. An explicit model is used to avoid employing matrices and inversion methods for the resolution of an equation system. The temperature variation over time is calculated by using temperatures at the previous time step. The spatial discretization uses a fixed grid.

$$\frac{\partial T}{\partial t} = \alpha \frac{\partial^2 T}{\partial x^2}$$

$$\frac{T_i^t - T_i^{t-1}}{dt} \approx \alpha \frac{T_{i-1}^{t-1} - 2T_i^{t-1} + T_{i+1}^{t-1}}{dx^2}$$

The heat equation in radial form is expressed in equation (6). A simple form in finite differences can be found in equation (7) [35].

$$\frac{\partial T}{\partial t} = \alpha \left(\frac{\partial^2 T}{\partial r^2} + \frac{\partial T}{r \partial r} \right)$$

$$\frac{T_i^t - T_i^{t-1}}{dt} \approx \alpha \frac{\left(1 - \frac{dx}{2r}\right)T_{i-1}^{t-1} - 2T_i^{t-1} + \left(1 + \frac{dx}{2r}\right)T_{i+1}^{t-1}}{dx^2}$$

Depending on the test, the time step increment dt is fixed to 10 s in general (or 3 s to facilitate convergence) and the dx element is fixed to 1 cm in general (or 2 mm for special comparison). The initial condition is a fixed temperature (of 15 °C for the capric-lauric mixture) in each node. At the first time step, the boundary conditions are a fixed temperature (of 19 °C for the capric-lauric mixture) at the heating element interface (Dirichlet condition) and an adiabatic wall at the other boundaries.

A spreadsheet is used for calculations of the simulation software. A melting temperature of 16 °C is assumed. If the component temperature is under the melting temperature, equations (5) or (7) are applied. The spreadsheet is organized in four tables, using time in lines and nodes in columns.

- Table I: temperature evolution
- Table II: net heat flows
- Table III: latent heat during the time step if fusion temperature is reached in table 1
- Table IV: cumulated latent heat over time until phase change is completed

Figure 2 presents an example of the simulation tool with the four tables. Properties are reported in the top left corner. Discretization parameters, boundary conditions and initial temperature are given below. This example operates with five nodes of 1 cm and a time step of 5 s. The table continues towards the bottom until time equals 21600 s (6

hours). Temperatures are presented on the graph over table I.

When melting temperature is reached, the heat flow difference, integrated over time in table III, enables to calculate the cumulated latent heat recovered by the component in table IV (equation (8)). When the cumulated latent heat equals the latent heat of complete fusion, the temperature continues to increase in table I. Phase change then occurs in the next component. These conditions are easily defined by min(), max(), sum() or if() functions of the spreadsheet software. They enable to reproduce the Stefan condition (equation (9)),

which calculates the position of the phase change interface s(t). (Density ρ is not specified as being liquid or solid phase density.) For PCM derived from coconut oil, thermal conductivities in liquid and solid phases are assumed equal (Table 1).

$$\Delta L = dt \left(\lambda_{comp,L} S_L \frac{T_{i-1}^{t-1} - T_i^{t-1}}{dx} - \lambda_{comp,S} S_S \frac{T_i^{t-1} - T_{i+1}^{t-1}}{dx} \right)$$

$$\rho L \frac{ds(t)}{dt} = \lambda_{comp,L} \frac{\delta T_L}{\delta t} - \lambda_{comp,S} \frac{\delta T_S}{\delta t}$$
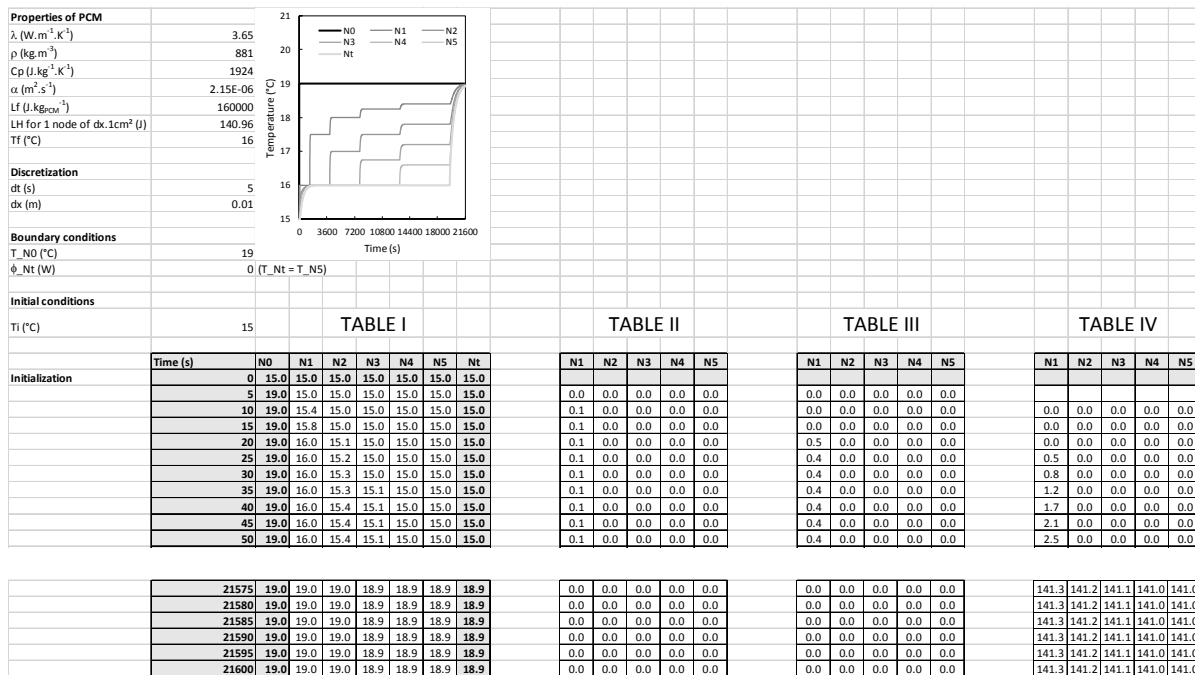
Properties of PCM

Property	Value
λ (W.m⁻¹.K⁻¹)	3.65
ρ (kg.m⁻³)	881
Cp (J.kg⁻¹.K⁻¹)	1924
α (m².s⁻¹)	2.15E-06
Lf (J.kg$_{PCM}$⁻¹)	160000
LH for 1 node of dx.1cm² (J)	140.96
Tf (°C)	16

Discretization

dt (s)	5
dx (m)	0.01

Boundary conditions

T_N0 (°C)	19
ϕ_Nt (W)	0 (T_Nt = T_N5)

Initial conditions

Ti (°C)	15

Time (s)	N0	N1	N2	N3	N4	N5	Nt	N1	N2	N3	N4	N5	N1	N2	N3	N4	N5	N1	N2	N3	N4	N5
			TABLE I							TABLE II					TABLE III					TABLE IV		
Initialization 0	15.0	15.0	15.0	15.0	15.0	15.0	15.0															
5	19.0	15.0	15.0	15.0	15.0	15.0	15.0	0.0	0.0	0.0	0.0	0.0	0.0	0.0	0.0	0.0	0.0					
10	19.0	15.4	15.0	15.0	15.0	15.0	15.0	0.1	0.0	0.0	0.0	0.0	0.0	0.0	0.0	0.0	0.0	0.0	0.0	0.0	0.0	0.0
15	19.0	15.8	15.0	15.0	15.0	15.0	15.0	0.1	0.0	0.0	0.0	0.0	0.0	0.0	0.0	0.0	0.0	0.0	0.0	0.0	0.0	0.0
20	19.0	16.0	15.1	15.0	15.0	15.0	15.0	0.1	0.0	0.0	0.0	0.0	0.5	0.0	0.0	0.0	0.0	0.0	0.0	0.0	0.0	0.0
25	19.0	16.0	15.2	15.0	15.0	15.0	15.0	0.1	0.0	0.0	0.0	0.0	0.4	0.0	0.0	0.0	0.0	0.5	0.0	0.0	0.0	0.0
30	19.0	16.0	15.3	15.0	15.0	15.0	15.0	0.1	0.0	0.0	0.0	0.0	0.4	0.0	0.0	0.0	0.0	0.8	0.0	0.0	0.0	0.0
35	19.0	16.0	15.3	15.1	15.0	15.0	15.0	0.1	0.0	0.0	0.0	0.0	0.4	0.0	0.0	0.0	0.0	1.2	0.0	0.0	0.0	0.0
40	19.0	16.0	15.4	15.1	15.0	15.0	15.0	0.1	0.0	0.0	0.0	0.0	0.4	0.0	0.0	0.0	0.0	1.7	0.0	0.0	0.0	0.0
45	19.0	16.0	15.4	15.1	15.0	15.0	15.0	0.1	0.0	0.0	0.0	0.0	0.4	0.0	0.0	0.0	0.0	2.1	0.0	0.0	0.0	0.0
50	19.0	16.0	15.4	15.1	15.0	15.0	15.0	0.1	0.0	0.0	0.0	0.0	0.4	0.0	0.0	0.0	0.0	2.5	0.0	0.0	0.0	0.0
21575	19.0	19.0	19.0	18.9	18.9	18.9	18.9	0.0	0.0	0.0	0.0	0.0	0.0	0.0	0.0	0.0	0.0	141.3	141.2	141.1	141.0	141.0
21580	19.0	19.0	19.0	18.9	18.9	18.9	18.9	0.0	0.0	0.0	0.0	0.0	0.0	0.0	0.0	0.0	0.0	141.3	141.2	141.1	141.0	141.0
21585	19.0	19.0	19.0	18.9	18.9	18.9	18.9	0.0	0.0	0.0	0.0	0.0	0.0	0.0	0.0	0.0	0.0	141.3	141.2	141.1	141.0	141.0
21590	19.0	19.0	19.0	18.9	18.9	18.9	18.9	0.0	0.0	0.0	0.0	0.0	0.0	0.0	0.0	0.0	0.0	141.3	141.2	141.1	141.0	141.0
21595	19.0	19.0	19.0	18.9	18.9	18.9	18.9	0.0	0.0	0.0	0.0	0.0	0.0	0.0	0.0	0.0	0.0	141.3	141.2	141.1	141.0	141.0
21600	19.0	19.0	19.0	18.9	18.9	18.9	18.9	0.0	0.0	0.0	0.0	0.0	0.0	0.0	0.0	0.0	0.0	141.3	141.2	141.1	141.0	141.0

Graph (Temperature (°C) vs Time (s)), legend: N0, N1, N2, N3, N4, N5, Nt.

Figure 2: Example of the simulation tool

Dutil et al. [34] regret that modelling sometimes neglects the effects of phenomena such as convection in the liquid phase (non-predominant in the CEG-PCM composite), thermal expansion, viscosity variation. Even though, to maintain the simulation tool's simplicity, some other simplifying hypotheses are assumed for the PCM or the EG-PCM composite, as reported in the following list.

- Convection in the liquid phase is assumed negligible. Only conduction is taken into account.
- Thermal properties of the PCM are constant.
- PCM is a pure substance.
- PCM is homogeneous and isotropic.
- Thermal expansion is neglected.
- Phase change is isothermal.

Only simulations of fusion are calculated by the software. When the chosen material has very close properties in liquid and solid phases, simulations of solidification should give roughly the same results under the same type of boundary conditions.

3.2 Model validation

The simulation model was validated using results from literature in different configurations, boundary conditions and phase change materials. Dutil et al. alert the scientific community on the lack of validation by experimental measurements [34]. The present 1D and radial models are validated using both simulations and experiments.

3.2.1 Validation of the 1D model

Younsi et al. present a validated simulation model using a salt hydrate as PCM in a 1D configuration [32]. The test section is heated at one side and cooled at the other side at a constant temperature of 15 °C. The fusion temperature is 27 °C. The initial temperature and the boundary temperature are 15 °C and 50 °C respectively. Distinct thermal properties for liquid and solid phases are here taken into account because they vary significantly for salt hydrates. Figure 3 shows the comparison of the fusion front displacement versus time. The present model does not take into account the convection in the liquid phase. Therefore, the heat transfer from the heating element to the fusion front is slightly reduced compared to the results obtained by Younsi et al.
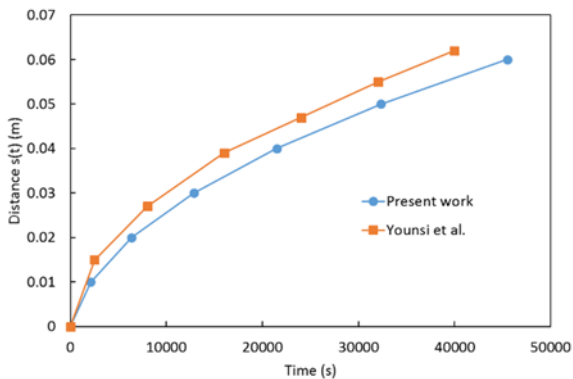
Figure 3: Comparison of the fusion front displacement with results of Younsi et al. [32]

Gasia et al. worked on a LHTES prototype using finned tubes with a fin pitch of 2 cm [29]. The corresponding simulation was run on a 1 cm test section divided into 5 elements (node N1 to node N5) of 2 mm each (left graph of figure 4). N0 (thick black line) is the boundary temperature equal to the average value of the red (Tin) and blue (Tout) temperatures of curves in the right-side graph of figure 4. T2, T5, T8, T11 and T14 of the right-side figure provide temperature evolutions at different positions in the experimental prototype volume of Gasia et al. Even though the model is only 1D and a constant temperature for phase change is assumed, evolutions are somewhat similar. Heat losses and convection heat transfer were also neglected in the model.

D'Avignon and Kummert worked with a commercial PCM having a melting temperature of 27 °C [27]. On the right graph of figure 5, the phase change temperature appears to be closer to 29 °C. This temperature was simulated using the present model to obtain the graph on the left. The temperature in node 0 is the boundary temperature. It was set to 37 °C at the first time step. Temperature evolutions through PCM of a half-thickness distance of 16 mm are in relative good agreement. The end of fusion seems to appear at the same time of around 2.5 hours. The differences between these two graphs derive mainly from the modelling assumption of an isothermal phase change, which is unrealistic in real compound products.
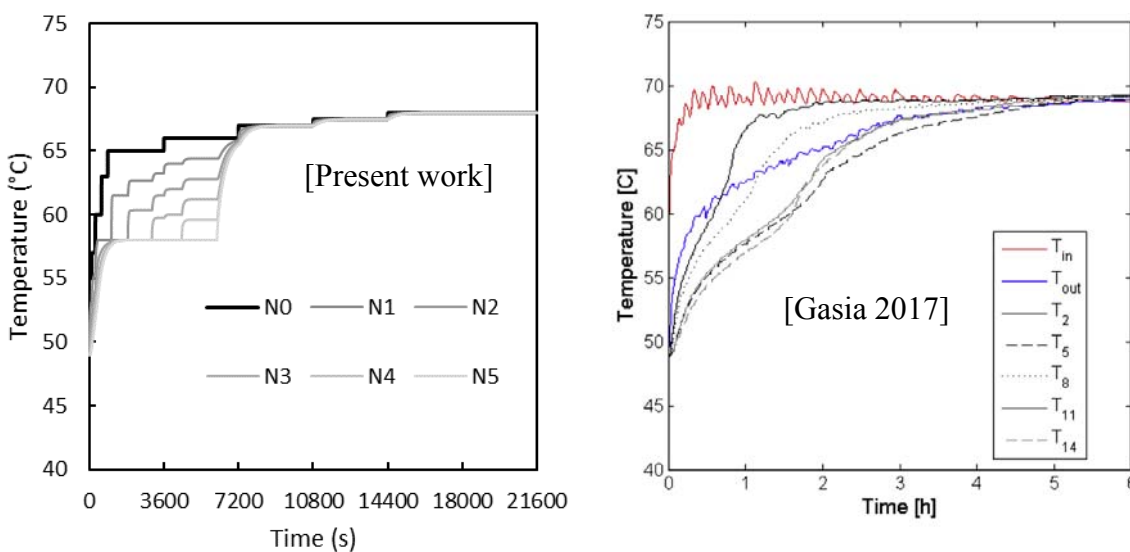
Figure 4: Comparison of temperature evolutions with results of Gasia et al. [29]
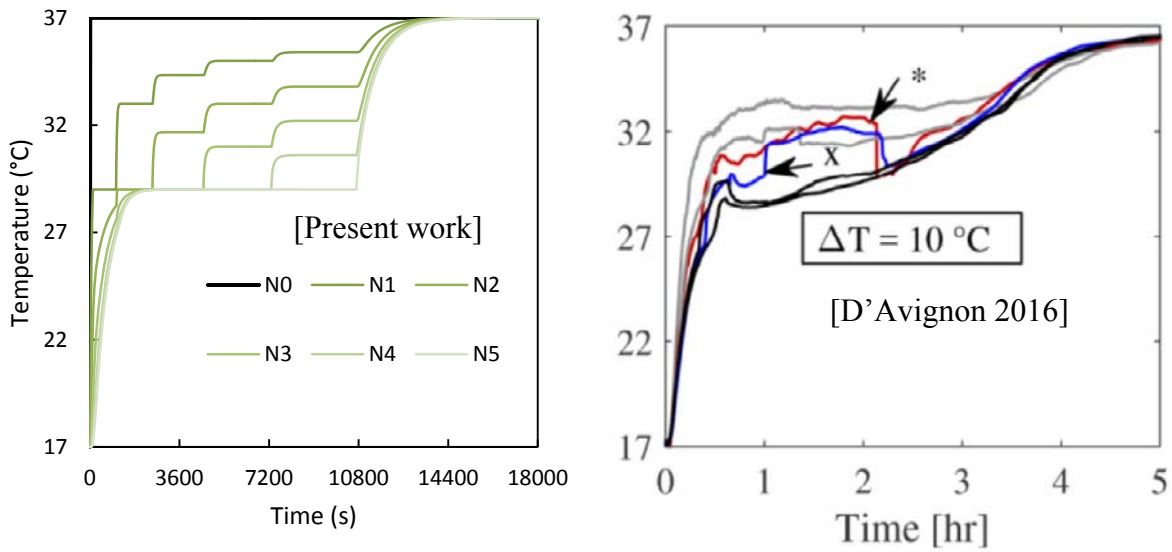
Figure 5: Comparison of temperature evolutions with results of D'Avignon and Kummert [27]

A second comparison with another result of the same publication pertains to power delivered to the PCM (figure 6). On the right-side graph, D'avignon and Kummert present repeated measurements of the evolutions of thermal power for 2 temperature differences between the heat transfer fluid inlet and the PCM melting point, and for 2 flow rates, 0.3 L/s and 0.45 L/s. Power decreases rapidly with time, figure 6 having a logarithmic scale on the x-axis. Such power decrease is due to the position of the fusion front moving away from the heat source. The heat flow needs to go through an increasing amount of liquid PCM before reaching the fusion front. Temperature gradients and heat flows decrease with time. Agyenim et al. [36] and Merlin [26] found the same behaviour in their experiments. In the left graph of figure 6, the simulation operates for a 10 K temperature difference with a time step of 10 s. The black line corresponds to the sum of the power over all nodes. The peak power is just underneath 30 kW, related to the entire stock of PCM. At 1000 s or 17 min, both graphs show a thermal power of 10 kW. At 10000 s or 167 min, the power similarly drops down to 2 kW on both graphs. The heat flux variation inside the PCM material also brings the question of a variable heat flux in the heat transfer fluid. A variable speed pump might be necessary to ensure a constant temperature difference on the distribution loop.
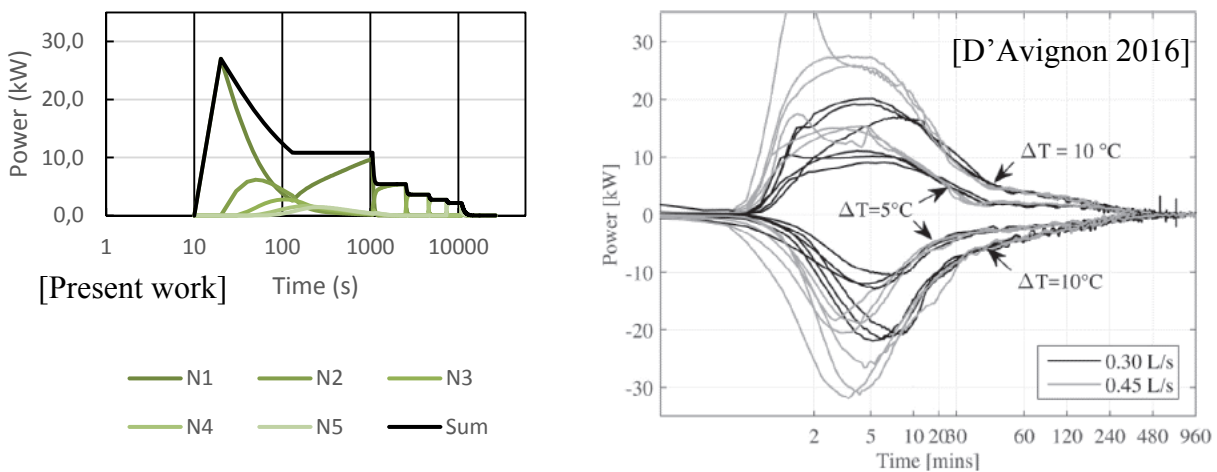
Figure 6: Comparison of power evolutions with results of D'Avignon and Kummert [27]

3.2.2 Validation of the radial model

The radial model is also compared to results from the literature. Youssef et al. worked with a spiral-wired tube and an organic paraffin type A16 [31]. They carried out experiments and computational fluid dynamics (CFD) simulations on this spiral-wired system using an effective thermal conductivity of 11.07 Wm-1.K-1. Eight tubes are arranged in a heat exchanger configuration. The tube diameter is 22 mm and the distance between two tubes is 72 mm (x-axis) or 73 mm (y-axis). The present simulation model uses components of 1 cm of portion of radius. The simulated tube outer diameter is 20 mm. The simulation area corresponds to a section of PCM or of PCM composite angled at 45 °, from the tube to adiabatic walls represented in figure 7. Nodes 1 and 2 are complete. Nodes 3 and 4 are reduced by the presence of the adiabatic wall. An area calculation enables to evaluate the amount of PCM contained in each node.

In figure 8, the present model shows results very close to the experimental results of Youssef et al. despite slight differences of dimensions. The right-side graph of figure 8 shows the increase of temperature in the centre of the heat exchanger made from spiral-wired tubes, at around 4 cm from the tube wall. It corresponds to node N4 in the simulation. The PCM starts to melt after 5 min (300 s) and melting ends after 30 min (1800 s), as the simulation predicts.
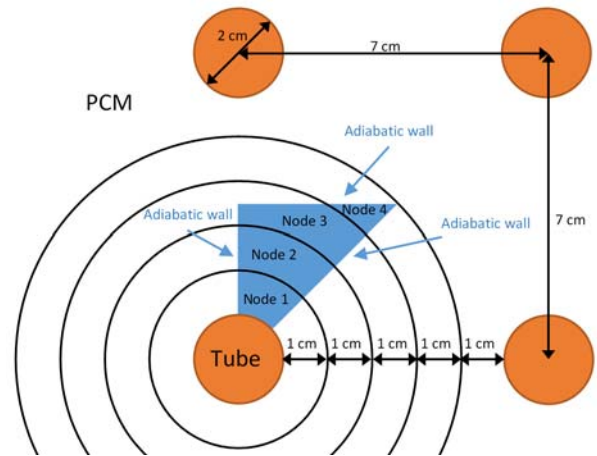
Figure 7: Simulation configuration in the case of the comparison with results of Youssef et al. [31]
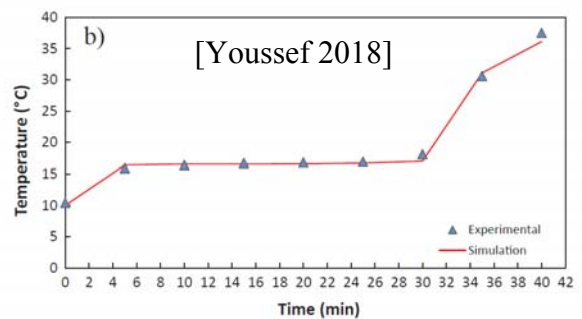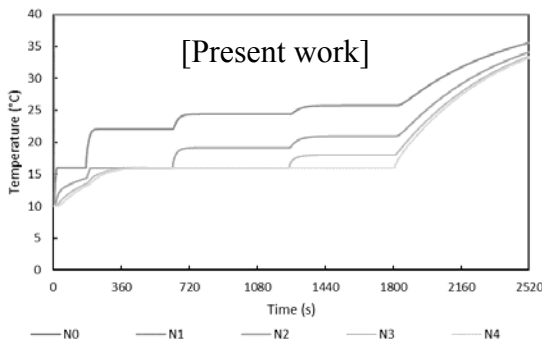
Figure 8: Comparison of temperature evolutions with results of Youssef et al. [31]

Other simulations are compared to results of Trp [30]. She used a technical grade paraffin Rubitherm RT 30 as PCM in a shell-and-tube configuration. In liquid phase, the PCM thermal conductivity is 0.19 W.m-1.K-1n, whereas its density is 750 kg.m-3. The outer tube diameter is 35 mm. The right-side graph of figure 9 shows the experimental and numerical results at a distance of 0.9 cm from the tube outer wall (r = 0.0265 m) and at distances of 35 cm (5) and 65 cm (9) from the tube entrance. The present model does not consider this variable as the wall temperature is assumed constant. On the left-side graph, nodes N0 and N1 (dotted lines) are considered to be part of the tube. N1 thickness was adjusted to 0.75 cm so that the cumulated thickness of N0 and N1 corresponds to the 1.75 cm outer radius of the tube. The grey-colour continuous curve of node N2 represents the PCM temperature increase at a distance of 1 cm from the tube outer wall (at a radius of 0.0275 m). It can be compared to the results of Trp. The other dotted lines (N3 to N6) represent temperature evolutions every centimetre further inside the PCM.
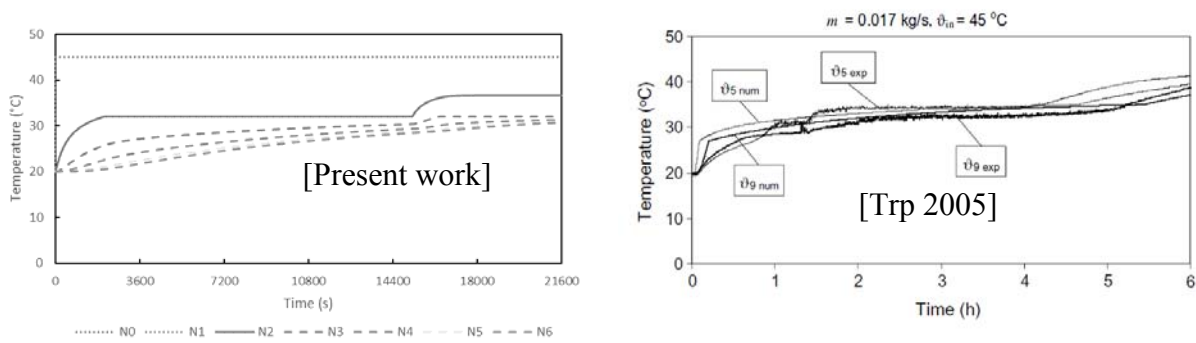
Figure 9: Comparison of temperature evolutions with results of Trp [30]

A part of Merlin's PhD thesis was to measure the temperature changes inside a CEG-PCM composite having an effective thermal conductivity of 22.2 W.m-1.K-1 with a graphite mass fraction of 25 %. Figure 10 shows the system configuration with five tubes and the distances between components [26]. The triangle corresponds to the simulation zone, and the circles to the boundaries of nodes in the radial direction. Figure 10 also describes the positions of the five temperature sensors used to plot temperatures, as per the right-side graph of figure 11. The actual outer tube diameter is 12 mm whereas the simulated diameter is 10 mm. The simulated boundary condition is a constant temperature of 85 °C. The isothermal fusion temperature is set to 68 °C.

Like in other simulations, the temperature of node N0 is the boundary temperature. N1 is closer to position 1 of experiment. Position 3 should have shown values similar to position 1. Merlin proposes to explain the difference by a position inaccuracy or by discrepancies in thermal contact [26]. The temperature change of node N2 corresponds roughly to those of positions 2 and 4, and temperature change of node N4, to change of position 5. The inflexion of the temperature curve at position 5 suggests that fusion ends after around 3 minutes and 30 seconds. The simulation result of end-of-fusion time is just below 4 minutes. This slight difference probably arises from the lower diameter of tubes and from the actual position of sensor 5, which is around 2 mm inside the outer circle of node N4.
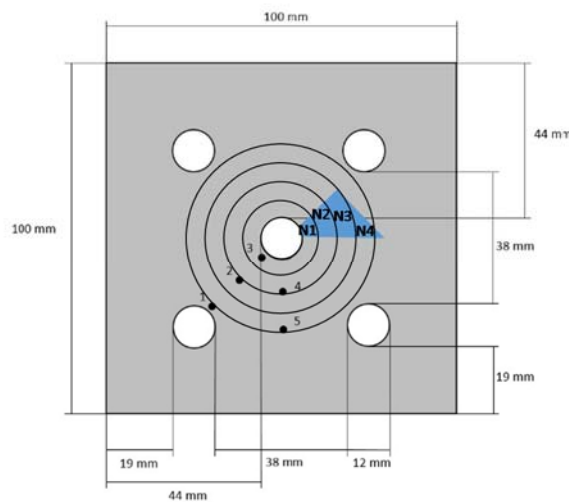
Figure 10: System configuration of Merlin [26] and arrangement of nodes for simulation
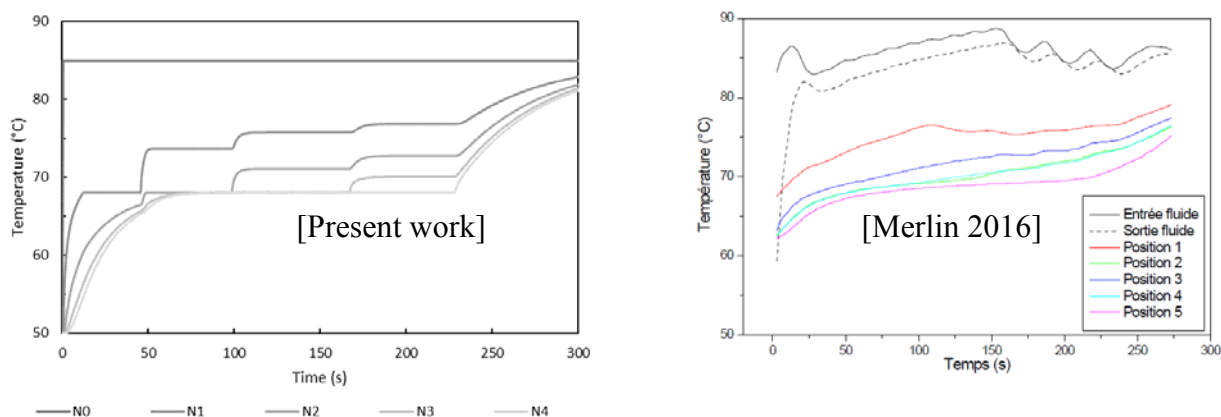
Figure 11: Comparison of temperature increases with results of Merlin [26]

3.2.3 Conclusion on model validation

The comparison of the unidimensional model simulations with results from the literature validates the equations and the assumptions for the cases studied with a salt hydrate PCM27 submitted to heat source at 50 °C and 37 °C, and with a paraffin RT58 submitted to a 70 °C boundary condition.

The comparison of the results of the radial model with three publications from the literature validates the transition from the unidimensional configuration to the radial configuration. The comparisons were led with paraffins having three different fusion temperatures. Conductivities of the composite or pseudo-composite materials were also varied.

The sensibility of the model to spatial discretization and to time step value was also tested. The model behaviour was found to be stable when varying time steps between 1 and 10 s and component sizes between 0.5 cm and 1 cm.

3.3 Simulation results

The simulation study is based on the following three LHTES configurations:

The shell-and-tube configuration with PCM being located in the shell and the heat transfer fluid being located in the tube (such as in figure 8 and figure 10).

The slab-like configuration where square or rectangular blocks of PCM are arranged in the volume of the tank and the heat transfer fluid flows on the sides of the blocks (such as in the study of D'Avignon and Kummert [27]).

The beam-like configuration, derived from the slab-like configuration, being heated on four sides instead of two.

3.3.1 Shell-and-tube configuration

The shell-and-tube system is tested considering the same tube spacing of 20 cm to limit the number of tubes in a full-scale LHTES, but while varying the tube diameter. The tube spacing being fixed at 20 cm in a square pattern, the adiabatic wall is located at the half of the spacing distance (10 cm). The furthest node from the tube is on the diagonal line at $10\sqrt{2}$ cm, rounded to 14 cm. Figure 12 presents the calculation zone for the shell-and-tube configuration. Figures 13 to 16 show the temperature increases for tube outer diameters of 20, 40, 60 and 80 mm. In figure 13, the tube diameter is 20 mm, so 13 nodes of 1 cm thickness (14 cm minus 10 mm of tube radius) are needed to reach the furthest part of the PCM. For a 40 mm diameter tube, node N1 is included in the tube. The temperature of this node is set to the boundary temperature. The same procedure is applied with nodes N2 and N3 for diameters of 60 mm and 80 mm respectively. Nodes N10 to N13 are limited by the adiabatic wall. The corresponding heat fluxes are reduced by an estimation of the node wall length with its neighbours. The corresponding latent heat needed to melt the PCM is also estimated by a volume calculation.

Properties of the PCM are reported in table 5. They are kept constant for this comparison. A latent heat (LH) of 117 J.cm-3 is estimated for a material using 83.6 % of PCM in volume. The time step is 3 s and the space element has a radius difference of 1 cm at a 45°. All nodes are initialized at 15 °C at starting time.
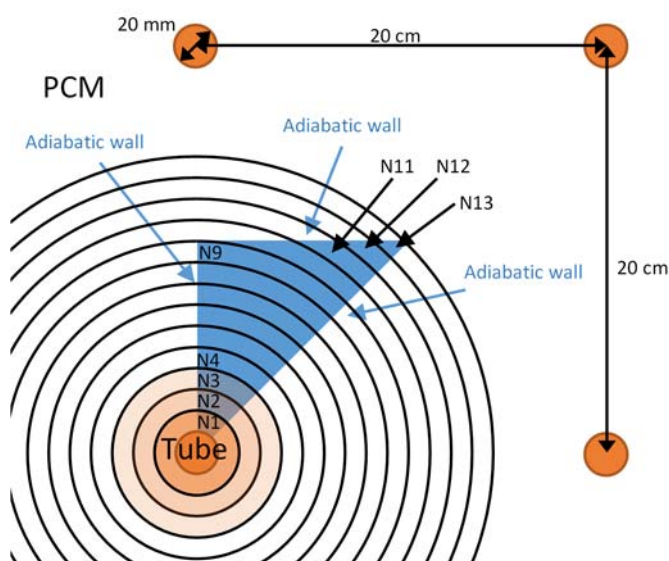
Figure 12: Calculation area for the shell-and-tube configuration

Table 5: Thermal properties of the EG-PCM composite for the shell-and-tube configuration

Property	Value
Fusion temperature	16 °C
Latent heat	117 J.cm^{-3}
Specific heat of solid and liquid	1803 J.kg^{-1}.K^{-1}
Density of solid and liquid	1003 kg.m^{-3}
Thermal conductivity of solid and liquid	20.09 W.m^{-1}.K^{-1}
Thermal diffusivity of solid and liquid	1.11×10^{-5} m^2.s^{-1}

Figures 13 and 14 show that the complete melting is not achieved. After 6 hours (21600 s), only 7 cm have melted with the 20 mm tube. N7 curve is the last one having lifted-up from the 16 °C plateau corresponding to the fusion temperature. For the 40 mm diameter tube, N10 curve has lifted-up from the plateau. As N1 is included in the tube, it means that 9 cm of PCM have melted.

Figure 15 describes the first complete melting of the PCM after around 4 hours and 45 minutes with a 60 mm diameter tube. When only liquid PCM is left in the composite material, the temperature reaches asymptotically the boundary temperature. The same pattern occurs faster, after around 3 hours and 20 minutes, with the 80 mm diameter tube. These results can be attributed to the two following reasons.

1. When the tube outer wall surface area is increased, the heat flux delivered to the PCM is higher.

2. A larger tube diameter impinges on the volume of PCM. A lesser amount of PCM leads to a shorter melting time.

60 mm seems a sufficient tube diameter for this shell-and-tube configuration. Increasing the tube diameter produces shorter melting times in these simulations with a perfect boundary condition. However, in practice, the flow rate of the heat transfer fluid has to be increased to guarantee the same heat transfer rate. Another drawback is the reduction of the actual volume for heat storage compared to the total volume of the system, decreasing by 6.1 % when increasing the tube diameter from 20 mm to 60 mm and by 11.4 % when increasing the tube diameter from 20 mm to 80 mm.
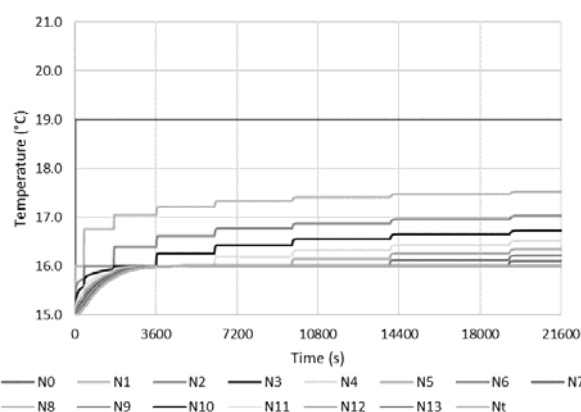

Figure 13: Increase of temperatures in a shell-and-tube configuration, tube of 20 mm diameter
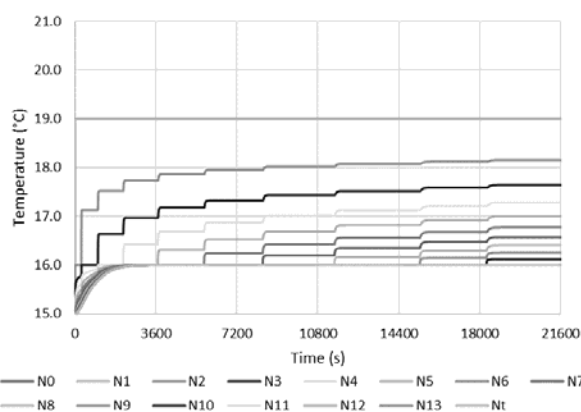

Figure 14: Increase of temperatures in a shell-and-tube configuration, tube of 40 mm diameter
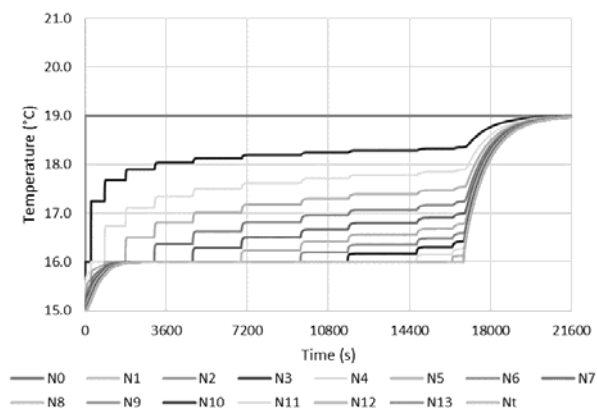
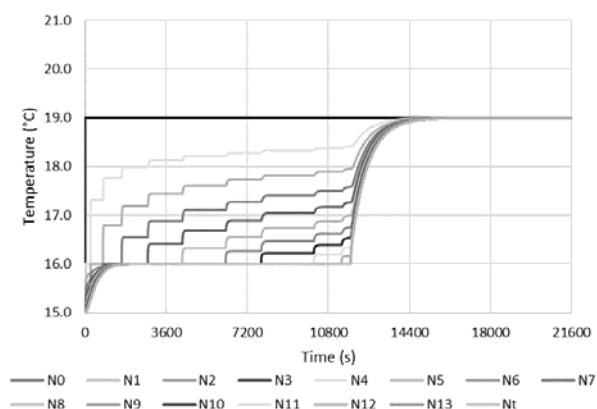**Figure 15: Increase of temperatures in a shell-and-tube configuration, tube of 60 mm diameter**

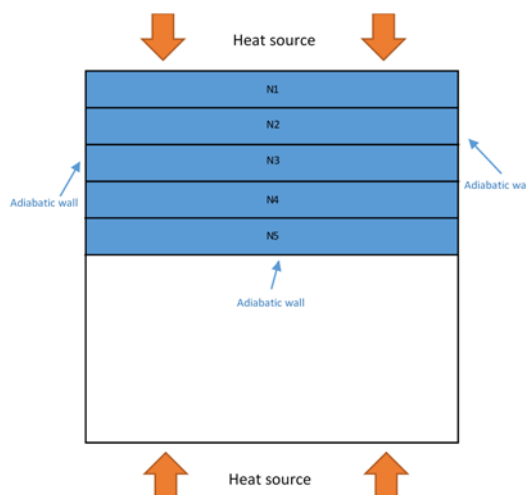**Figure 16: Increase of temperatures in a shell-and-tube configuration, tube of 80 mm diameter**

Figure 17: Scheme of the simulation zone of the slab-like model
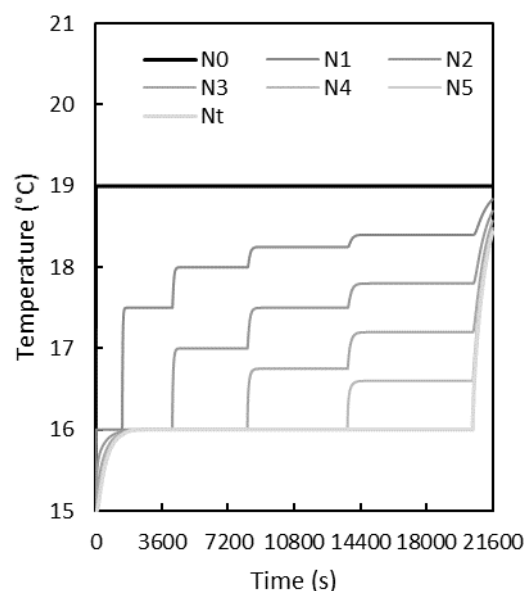
Figure 18: Simulation of the slab-like configuration with pure PCM

3.3.2 Slab-like configuration

The slab-like configurations use the unidimensional model according to figure 17. The objective of this part of the simulation study is to determine the maximum thickness allowed for the complete melting of a pure PCM, of a PCM with a low-carbon loading and of a composite of PCM and compressed expanded graphite. Thermal conductivities are 0.18, 3.65 and 20.09 $W.m^{-1}.K^{-1}$ respectively (table 4).

Figure 18 shows the increase of temperatures, using the 1D model for a pure PCM. Node N1 is in contact with the heat source and N5 corresponds to the symmetry axis or adiabatic wall. The maximum allowed thickness was found by iterations. A dimension dx of 2.4 mm is the upper limit to completely melt the pure PCM slab within a 6-hour span. It corresponds to a 24 mm slab thickness (5 nodes of 2.4 mm heated from both sides).

Figure 19 presents the results with a light carbon loading of 5 % in mass. The mixture properties come from table 4. In this configuration, the maximum allowed thickness rises to 11 cm. Even though conductivity is almost multiplied by a factor 20, maximum thickness is only multiplied by a factor 4.6. Figure 20 shows that the maximum allowed thickness for complete melting is 26.3 cm in the case of the CEG-PCM composite. As heat transfers through the PCM, more and more nodes melt. However, the thermal resistance between the heating component and the melting node increases. Therefore, the heat flux decreases and the melting time increases. When the material thickness

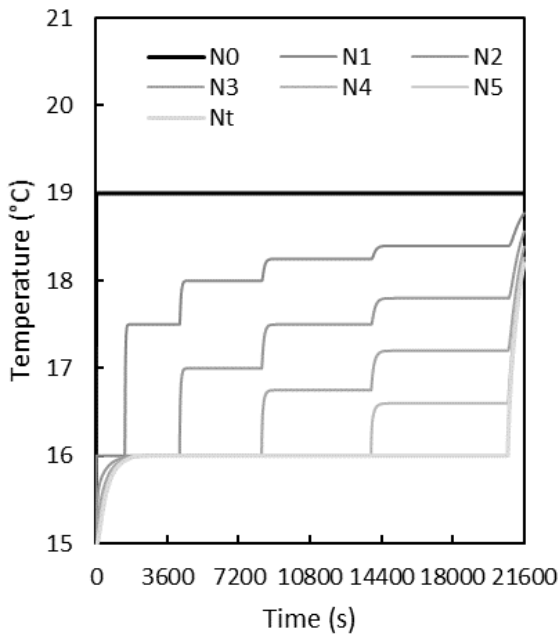doubles, the complete melting time is roughly multiplied by a factor 4.

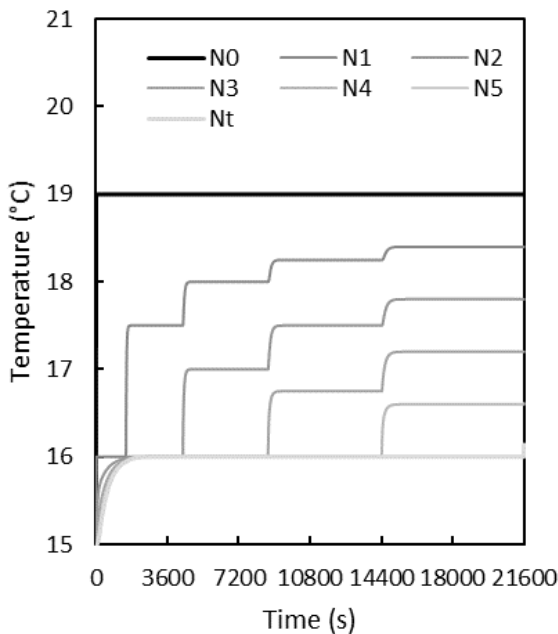**Figure 19: Simulation of the slab-like configuration with PCM plus low carbon loading**

Figure 20: Simulation of the slab-like configuration with CEG-PCM composite

3.3.3   Beam-like configuration

The beam-like configuration is presented in figure 21 for a square beam. The simulation area takes a triangle shape since the heat source acts on all four sides of the beam. As the node number increases, volume decreases. The heat fluxes through each node is recalculated according to the

heat exchange surface. The edge length is varied between 30 cm and 42 cm by changing the node depth. The simulations are operated with the CEG–PCM composite material, using 15 nodes at each occasion.
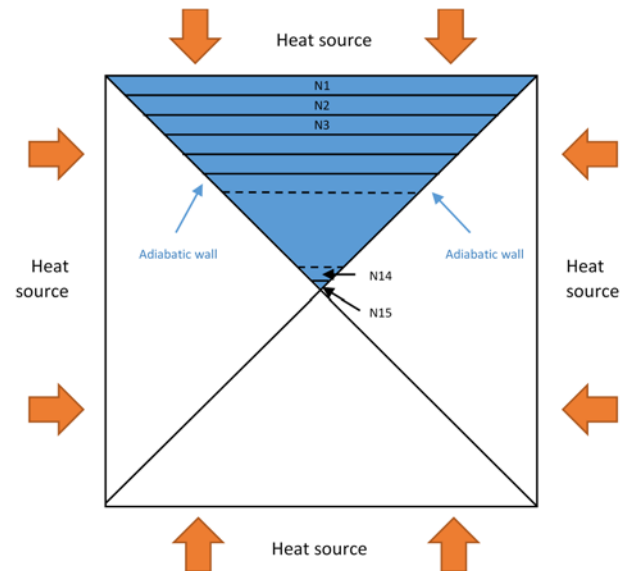

Figure 21: Scheme of the beam-like configuration heated on four surfaces.

Figure 22 presents the simulation results for a square beam heated from four sides. The increase of melting time with respect to material thickness appears less dramatic than in the slab-like configuration. Between the 3600 s and 7200 s time span, the average time interval between the end of melting of two consecutive nodes are 17, 23, 27 and 29 minutes when the node depth varies from 1 cm to 1.4 cm. According to these simulations, beams with edge length between 30 cm and 39 cm would satisfy the criterion of complete phase change within 6 hours. The complete melting time of beams with an edge length of 42 cm occurs at a time of 6 hours and 43 minutes.

3.4   Simulation summary

Three configurations of LHTES were identified as realizable at a full scale for hotels and tested with the simulation tool. A 60 mm tube diameter for the shell-and-tube configuration seemed the most interesting because the criterion of complete melting within 6 hours was satisfied and because the tube did not impinge too much on the PCM volume. Another limitation could arise regarding the heat transfer coefficient inside the tube. The study in the slab-like configuration concludes to the necessary use of CEG-PCM for slabs of over 20 cm thickness. Low carbon loading would allow slabs of 10 cm thickness. However, the thermal resistance of the encapsulation material was not taken into account

and will surely affect the system performance. The beam-like configuration appears interesting if a bottleneck appears on the heat transfer surface area, on the heating fluid side. A 30 cm x 30 cm beam has the same volume as a 23 cm x 39 cm slab, whereas the beam's heat transfer area is 53 % higher than the slab's.
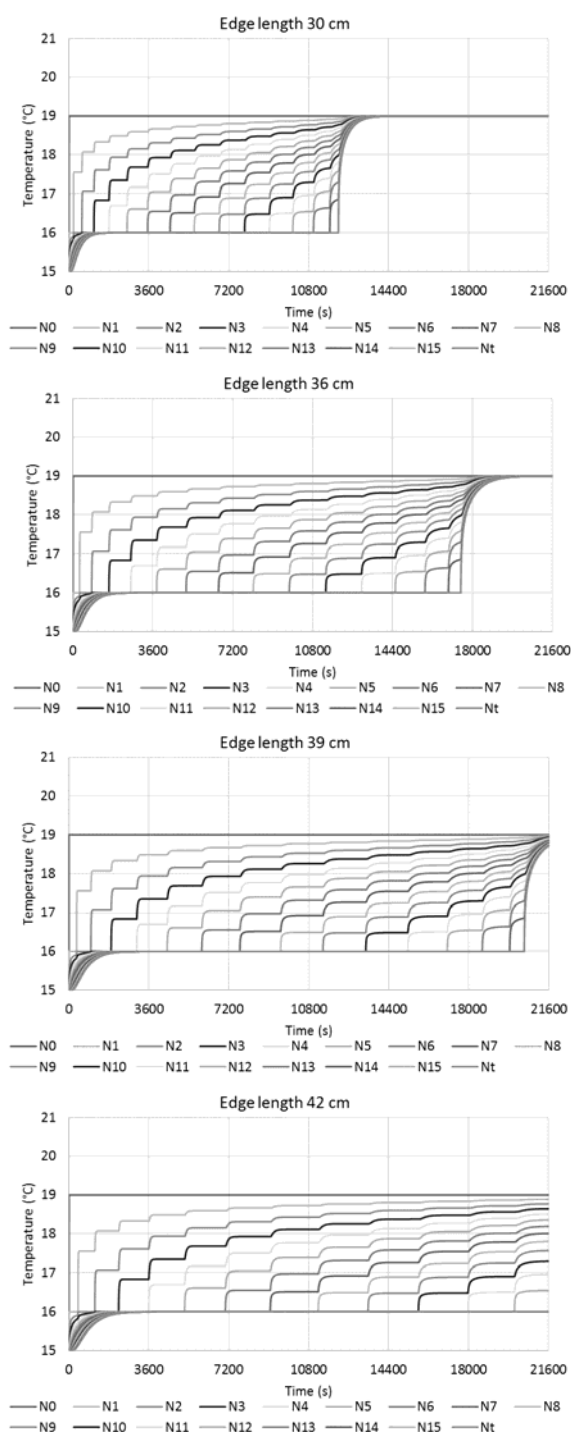

Figure 22: Simulations of the square beam-like configuration for edge lengths of 30, 36, 39 and 42 cm

4 Conclusion

A literature review concluded to the necessity of using a PCM material to store latent heat in the application of solar air-conditioning for a net-zero energy hotel. The selected PCM is a eutectic mixture of two fatty acids derived from coconut oil for commercial reasons. However, its low thermal conductivity needs to be enhanced. A compressed expanded graphite matrix was chosen for cost reasons.

A simple simulation tool was developed using the finite difference method. Researchers or design engineers can easily use this model to quickly assess the complete melting time of a PCM mass. The model validation proves that it could operate with different phase change materials, in 1D or radial, with different time steps or component sizes and under different boundary conditions. Several configurations for a full-scale LHTES were simulated: shell-and-tube with a spacing of 20 cm, a slab-like configuration and a beam-like configuration. All three configurations can be implemented in a LHTES even though the beam-like configuration seems more interesting in terms of heat transfer area. The final choice will depend on technical and economic reasons that the authors were not yet able to study. Prototyping will be the next step. The next study will specifically focus on the interface between the heat transfer fluid and the CEG-PCM composite material. The constant boundary condition has to be respected as much as possible.

This study proves that storing cooling energy in a LHTES for large buildings is possible at reasonable cost. It offers a path towards off-grid hotels in warm places as well as towards related applications of heat storage such as fatal energy from industrial plants.

Acknowledgements

References

[1] Vakiloroaya V., Samali B., Fakhar A., Pishghadam K. A review of different strategies for HVAC energy saving, Energy Conversion and Management 77 (2014) 738–754

[2] Isaac M., van Vuuren D.P. Modeling global residential sector energy demand for heating

and air conditioning in the context of climate change, Energy Policy 37 (2009) 507–521

[3] Shiming D., Burnett J. Energy use and management in hotels in Hong Kong, Hospitality Management 21 (2002) 371–380

[4] Bie Y., Li M., Malekian Reza, Chen F., Feng Z., Li Z. Effect of phase transition temperature and thermal conductivity on the performance of Latent Heat Storage System, Applied Thermal Engineering 135 (2018) 218–227

[5] Li H., Wang S., Cheung H. Sensitivity analysis of design parameters and optimal design for zero/low energy buildings in subtropical regions, Applied Energy 228 (2018) 1280–1291

[6] D'Agostino D., Zacà I., Baglivo C., Congedo P.M. Economic and thermal evaluation of different uses of an existing structure in a warm climate, Energies 2017, 10, 658

[7] Kohlenbach P., Osborne J., Jakob U. Photovoltaic vs solar thermal cooling: a comparison for Europe, 10th Gustav Lorentzen Conference, Delft, The Nederlands (2012) GL-264

[8] Zhang Y., Zhou G., Lin K., Zhang Q., Di H. Application of latent heat thermal energy storage in buildings: State-of-the-art and outlook, Building and Environment 42 (2007) 2197–2209

[9] Lizana J., Chacartegui R., Barrios-Padura A., Valverde J.M. Advances in thermal energy storage materials and their applications towards zero energy buildings: A critical review, Applied Energy 203 (2017) 219–239

[10] Hasnain S.M. Review on sustainable thermal energy storage technologies, part II: Cool thermal storage, Energy Conversion Management 39 (1998) 1139-1153

[11] Bourne S., Novoselac A. Improved performance in tube-encapsulated phase change thermal energy stores for HVAC applications, Building and Environment 98 (2016) 133-144

[12] Luthander R., Widen J., Nilsson D., Palm J. Photovoltaic self-consumption in buildings: A review, Applied energy 142 (2015) 80-94

[13] Feldman D., Shapiro M.M., Banu D., Fuks C.J. Fatty acids and their mixtures as phase change materials for thermal energy storage, Solar Energy Materials 18 (1989) 201-216

[14] Longfei J., Fengping X. Phase diagram of the ternary system lauric acid–capric acid–naphthalene, Thermochimica Acta 424 (2004) 1-5

[15] Fauzi H., Metselaar H.S.C., Mahlia T.M.I., Silakhori M. Sodium laurate enhancements the thermal properties and thermal conductivity of eutectic fatty acid as phase change material (PCM), Solar Energy 102 (2014) 333-337

[16] Badenhorst H. A review of the application of carbon materials in solar thermal energy storage, Solar Energy (Status: in press, corrected proofs) (2018) https://doi.org/10.1016/j.solener.2018.01.062

[17] Lin Y., Jia Y., Alva G., Fang G. Review on thermal conductivity enhancement, thermal properties and applications of phase change materials in thermal energy storage, Renewable and Sustainable Energy Reviews 82 (2018) 2730–2742

[18] Putra N., Amin M., Kosasih E.A., Achmad Luanto R. Abdullah N.A. Characterization of the thermal stability of RT 22 HC/graphene using a thermal cycle method based on thermoelectric methods, Applied Thermal Engineering 124 (2017) 62-70

[19] Mallow A., Abdelaziz O., Graham Jr. S. Thermal charging study of compressed expanded natural graphite/phase change material composites, Carbon 109 (2016) 495-504

[20] Krzesinska M., Lachowski A.I. Elastic properties of monolithic porous blocks of compressed expanded graphite related to their specific surface area and pore diameter, Materials Chemistry and Physics 86 (2004) 105–111

[21] Krzesinska M. Influence of the raw material on the pore structure and elastic properties of compressed expanded graphite blocks, Materials Chemistry and Physics 87 (2004) 336–344

[22] Souayfane F., Fardoun F., Biwole P.H. Phase change materials (PCM) for cooling applications in buildings: A review, Energy and Buildings 129 (2016) 396–431

[23] Tay N.H.S., Liu M., Belusko M., Bruno F. Review on transportable phase change material in thermal energy storage systems, Renewable and Sustainable Energy Reviews 75 (2017) 264–277

[24] Pardinas A.A., Alonso M.J., Dizc R., Husevåg Kvalsvik K., Fernández-Seara J. State-of-the-art for the use of phase-change materials in tanks coupled with heat pumps, Energy and Buildings 140 (2017) 28–41

[25] Mohamed S.A., Al-Sulaiman F.A., Ibrahim N.I., Zahir M.H., Al-Ahmed A., Saidur R.,

Yılbaş B.S., Sahin A.Z. A review on current status and challenges of inorganic phase change materials for thermal energy storage systems, Renewable and Sustainable Energy Reviews 70 (2017) 1072–1089

[26] Merlin K. Caractérisation thermique d'un matériau à changement de phase dans une structure conductrice, PhD Thesis, Université de Nantes, 2016

[27] D'Avignon K., Kummert M. Experimental assessment of a phase change material storage tank, Applied Thermal Engineering 99 (2016) 880–891

[28] Fornarelli F., Camporeale S.M., Fortunato B. Simplified theoretical model to predict the melting time of a shell-and-tube LHTES, Applied Thermal Engineering 153 (2019) 51-57

[29] Gasia J., Diriken J., Bourke M., Van Bael J., Cabeza L.F. Comparative study of the thermal performance of four different shell-and-tube heat exchangers used as latent heat thermal energy storage systems, Renewable Energy 114 (2017) 934-944

[30] Trp A. An experimental and numerical investigation of heat transfer during technical grade paraffin melting and solidification in a shell-and-tube latent thermal energy storage unit, Solar Energy 79 (2005) 648–660

[31] Youssef W., Ge Y.T., Tassou S.A. CFD modelling development and experimental validation of a phase change material (PCM) heat exchanger with spiral-wired tubes, Energy Conversion and Management 157 (2018) 498–510

[32] Younsi Z., Joulin A., Zalewski L., Lassue S., Rousse D. Analyse numérique de la fusion de matériaux à changement de phase dans une enceinte rectangulaire chauffée par une paroi latérale, Proceedings of colloque CIFQ 2009, Lille, France, 165-170

[33] Bhattacharya A., Calmidi V.V., Mahajan R.L. Thermophysical properties of high porosity metal foam. International Journal of Heat and Mass Transfer 45 (2002) 1017–31.

[34] Dutil Y., Rousse D.R., Ben Salah N., Lassue S., Zalewski L. A review on phase-change materials: Mathematical modeling and simulations, Renewable and Sustainable Energy Reviews 15 (2011) 112–130

[35] Horbaniuc B., Dumitrascu G., Dumencu A. Étude du stockage thermique dans le sol en utilisant un schéma à différences finies unidimensionnel, Termotehnica 1 (2014) 42-47

[36] Agyenim F. Eames P., Smyth M. Heat transfer enhancement in medium temperature thermal energy storage system using a multitube heat transfer array, Renewable Energy 35 (2010) 198–207

Nomenclature

Abbreviations:
AC — air-conditioning
CEG — compressed expanded graphite
EG — expanded graphite
LH — latent heat
LHTES — latent heat thermal energy storage
N — node
PCM — phase change material
PV — photovoltaic

Latin letters:
Cp — specific heat, $J.kg^{-1}.K^{-1}$
dt — time step, s
dx — element length, m
dr — radial element length, m
L — latent heat, J
r — radius, m
s — fusion front position, m
S — surface area, m^2
T — temperature, °C

Greek letters:
α — thermal diffusivity, $m^2.s^{-1}$
ϕ — heat flux, W
λ — thermal conductivity, $W.m^{-2}.K^{-1}$
ρ — density, $kg.m^{-3}$

Superscript:
t — time increment

Indices:
comp — composite
EG — expanded graphite
i — number of node or initial
f — fusion
L — liquid
S — solid
t — terminal
X — series model
|| — parallel model